Reduced Hysteresis and Enhanced Giant Magnetocaloric Effect in B-Doped all- d -Metal Ni - Co - Mn - Ti -Based Heusler Materials

Zhang, Fengqi; Batashev, Ivan; Van Dijk, Niels; Bruck, Ekkes

DOI
10.1103/PhysRevApplied.17.054032

Publication date
2022

Document Version
Final published version

Published in
Physical Review Applied

Reduced Hysteresis and Enhanced Giant Magnetocaloric Effect in B-Doped all-*d*-Metal Ni-Co-Mn-Ti-Based Heusler Materials

Fengqi Zhang,* Ivan Batashev, Niels van Dijk, and Ekkes Bruck
Fundamental Aspects of Materials and Energy (FAME), Faculty of Applied Sciences, Delft University of Technology, Mekelweg 15, 2629JB Delft, Netherlands

(Received 26 January 2022; accepted 26 April 2022; published 19 May 2022)

The all-*d*-metal Ni-(Co)-Mn-Ti-based Heusler alloys are found to show a giant magnetocaloric effect near room temperature and are thereby potential materials for solid-state refrigeration. However, the relative large thermal hysteresis and the moderate ferromagnetic magnetization provides limitations for real applications. In the present study, we demonstrate that introducing interstitial B atoms within $Ni_{36.5}Co_{13.5}Mn_{35}Ti_{15}$ alloys can effectively decrease the thermal hysteresis ΔT_{hys} (down to 4.4 K), and simultaneously improve the saturation magnetization (maximum 40% enhancement) for low concentrations of B doping (up to 0.4 at. %). In comparison to the undoped reference material, the maximum magnetic entropy change (ΔS_m) for the $Ni_{36.5}Co_{13.5}Mn_{35}Ti_{15}B_{0.4}$ alloy shows a remarkable improvement from 9.7 to 24.3 J kg^{-1} K^{-1} for an applied magnetic field change ($\Delta\mu_0 H$) of 5 T (30.2 J kg^{-1} K^{-1} for $\Delta\mu_0 H = 7$ T). Additionally, due to the obtained low thermal hysteresis ΔT_{hys}, the maximum reversible ΔS_m^{rev} amounts to 18.9 J kg^{-1} K^{-1} at 283 K for $\Delta\mu_0 H = 5$ T (22.0 J kg^{-1} K^{-1} at 281 K for $\Delta\mu_0 H = 7$ T), which is competitive to the traditional Ni-Mn-X-based Heusler alloys (X = Ga, In, Sn, Sb). The enhancement of the magnetic moments by B doping is also observed in first-principles calculations. These calculations clarify the atomic occupancy of B and the changes in the electronic configuration. Our current study indicates that interstitial doping with a light element (boron) is an effective method to improve the magnetocaloric effect in these all-*d*-metal Ni-Co-Mn-Ti-based magnetic Heusler compounds.

DOI: 10.1103/PhysRevApplied.17.054032

I. INTRODUCTION

Magnetocaloric materials (MCMs), which hold a giant magnetocaloric effect (GMCE), enable promising application scenarios such as solid-state magnetic refrigeration [1], magnetic heat pumps [2], and thermomagnetic generators to covert low-temperature waste heat to electricity [3]. In comparison to the conventional magnetocaloric effect (MCE), the "giant" MCE arises from an efficient coupling of different degrees of freedom (e.g., magnetic spin order-disorder, structural transformations, phonon excitations, or changes in electronic state). The GMCE results in a large isothermal entropy change composed from magnetic, lattice, and electronic contributions [4]. Depending on the type of coupling, the MCMs can be distinguished in magnetoelastic and magnetostructural MCMs. The magnetoelastic MCMs are mainly represented by $(Mn,Fe)_2(P,X)$-based (X = As, Ge, Si) [5], $La(Fe,Si)_{13}$-based [6], Fe-Rh-based [7], and Eu_2In [8] compounds, while the magnetostructural MCMs are mainly found in $Gd_5(Si_2Ge_2)$ [9], Ni-Mn-X-based magnetic Heusler alloys (X = Ga, In, Sn, Sb) [10] and Mn-M-X (M = Co or Ni, X = Si or Ge) ferromagnets [11,12].

Among these MCMs the Ni-Mn-X-based Heusler alloys (X = Ga, In, Sn, Sb) attract significant attention because of their fruitful multifunctionality with, e.g., caloric effects [1] (magnetocaloric, elasticaloric, barocaloric, multicaloric), giant magnetoresistance [13], and exchange bias [14]. Aside from the traditional Ni-Mn-based Heusler alloys, which are stabilized by *p*-*d* hybridization, the all-*d*-metal Ni-(Co)-Mn-Ti-based Heusler alloys functionalized by *d*-*d* covalent hybridization were successfully introduced. This resulted in an obvious enhancement of the mechanical properties across the martensitic transition where the intrinsic brittleness of the traditional Heusler alloys could efficiently be prevented [15,16]. Encouraged by this progress, some studies have been reported to further optimize the experimental MCE performance, in combination with electronic structure calculations [17,18]. For example, by applying a rapid-solidification technique (melt spinning) Bez and coworkers demonstrated that $Ni_{37.5}Co_{12.5}Mn_{35}Ti_{15}$ ribbons show a magnetic entropy change (ΔS_m) as high as 27 J kg^{-1} K^{-1} for a moderate magnetic field change ($\Delta\mu_0 H$) of 2 T [19]. Simultaneously, Taubel and coworkers reported that an optimized heat treatment can significantly affect the magnetocaloric properties in $Ni_{35}Co_{15}Mn_{37}Ti_{13}$ with a ΔS_m of 20 J kg^{-1} K^{-1} and a maximum adiabatic temperature change (ΔT_{ad}) of

*f.zhang-7@tudelft.nl

−4 K for $\Delta\mu_0 H = 1.93$ T [20]. Combining a MCE with hydrostatic pressures or uniaxial stresses can result in an enhanced magnetocaloric performance through a multicaloric cycle [21,22]. However, a relatively large thermal hysteresis (10–40 K) is observed in the above mentioned materials, which will dramatically reduce the heating and cooling efficiency in a practical thermodynamic cycle, which compromises the advantages (excellent mechanical properties [23], rare-earth-free composition and nontoxicity) of these all-*d*-type Heusler alloys. Additionally, apart from the current so-called "Co ferromagnetism activation effect," there are no other known substitutions that can efficiently optimize the ferromagnetic ordering.

Consequently, inspired by the effect of doping with light elements (e.g., B, C, N) in other MCM systems [24–29], in the present study interstitial B doping is investigated. A series of $Ni_{36.5}Co_{13.5}Mn_{35}Ti_{15}B_x$ ($x = 0$, 0.2, 0.4, 0.6, and 0.8) alloys is successfully produced and their thermodynamic, magnetic, GMCE properties are reported. Density-functional theory (DFT) modeling is applied to determine the atomic occupancy of B and theoretical electron localization function (ELF) calculations provide information on the changes in electronic environment in the surroundings of the main atoms. Our current study demonstrates the positive influence of interstitial B doping for the all-*d*-metal Ni-(Co)-Mn-Ti-based Heusler alloys and shows how B affects the GMCE performance, which deepens our understanding of this all-*d*-metal-type Heusler system.

II. METHODS AND EXPERIMENTAL PROCEDURE

High-purity (99.9%) raw materials are used to prepare polycrystalline samples with a nominal composition of $Ni_{36.5}Co_{13.5}Mn_{35}Ti_{15}B_x$ ($x = 0$, 0.2, 0.4, 0.6, and 0.8) using the arc-melting method under Ar atmosphere. The samples are melted for 5 times. To compensate the overevaporation of Mn during melt processing, 4 at. % extra Mn are introduced. To ensure the homogeneity the as-cast ingots are sealed in quartz ampoules under 20-kPa Ar and annealed at 1173 K for 6 days in a vertical furnace and then quickly quenched into cold water.

Zero-field differential scanning calorimetry (DSC) measurements are carried out using a commercial TA-Q2000 DSC calorimeter. The DSC measurements under different applied magnetic fields (up to 1.5 T) are performed in a home-built Peltier cell-based DSC, where the calorimetric ΔS_m and ΔT_{ad} are derived from specific heat measurements [30,31].

X-ray diffraction (XRD) patterns at different temperatures are collected using an Anton Paar TTK450 temperature-tunable sample chamber and a PANalytical X-pert Pro diffractometer with Cu Kα radiation. The XRD patterns are processed using Fullprof's implementation of the Rietveld refinement method [32].

Temperature-dependent magnetization (*M*-*T*) and field-dependent magnetization (*M*-*H*) curves are measured in a superconducting quantum interference device (SQUID, Quantum Design MPMS 5XL) magnetometer. The so-called loop method is used for isothermal *M*-*H* measurements at different temperatures to eliminate the influence of thermal history [33]. The samples are initially cooled down to 200 K (the complete martensite region) and then subsequently heated to the target temperature at a rate of 2 K/min.

DFT calculations are performed using the Vienna *ab initio* simulation package (VASP) [34,35]. The ion-electron interactions are described via the projector augmented-wave (PAW) [36,37] method and the generalized gradient approximation of Perdew-Burke-Ernzerhof [38] is used for the exchange correlation functional. 3*d* and 4*s* electrons are treated as valence electrons for Ni and Co. 3*d*, 3*p*, and 4*s* for Mn, and 3*s*, 3*p*, 3*d*, 4*s* for Ti, while for B 2*s* and 2*p* are set as valence electrons. A $2 \times 2 \times 1$ supercell based on a 16-atom unit cell is relaxed on a γ-centered **k**-grid of $6 \times 6 \times 9$ using the Methfessel-Paxton method of the second order [39] with a smearing width of 0.05 eV (*B*2 austenite structure with partial disorder of excess Mn and Ti is considered). The kinetic energy cutoff is set at 520 eV with the force convergence criteria at 0.1 meV/Å and convergence criteria of the energies at 1 μeV.

To deduce the site preference, the formation energies of the structures with a B atom placed on several possible crystallographic sites are compared. The energy cost corresponding to each structure is calculated as the difference between energies of doped (E_{doped}) and pure (E_{pure}) compounds minus the chemical potential of boron (μ_d) plus the chemical potential of the atom substituted by boron (μ_s).

$$E_f = E_{doped} + \mu_s - (E_{pure} + \mu_d). \quad (1)$$

To study the changes in the electronic environment the ELF is analyzed [40]. The ELF allows for accurate characterization of the bond nature based on electron densities. This characterization is based on topological analysis of local quantum-mechanical functions related to the Pauli exclusion principle. ELF effectively states the possibility of finding a second electron with the same spin close to where the reference electron is located. High ELF values point to areas with more localized electrons and indicate stronger covalent bonding.

III. RESULTS AND DISCUSSIONS

The zero-field DSC curves of the $Ni_{36.5}Co_{13.5}Mn_{35}Ti_{15}B_x$ ($x = 0.0$, 0.2, 0.4) alloys are shown in Fig. 1(a). Sharp exothermic and endothermic peaks indicate the presence of a first-order phase transition. The corresponding characteristic temperatures (A_s, A_f, M_s, M_f), thermal hysteresis (ΔT_{hys}), transformation entropy changes (ΔS_{tr})

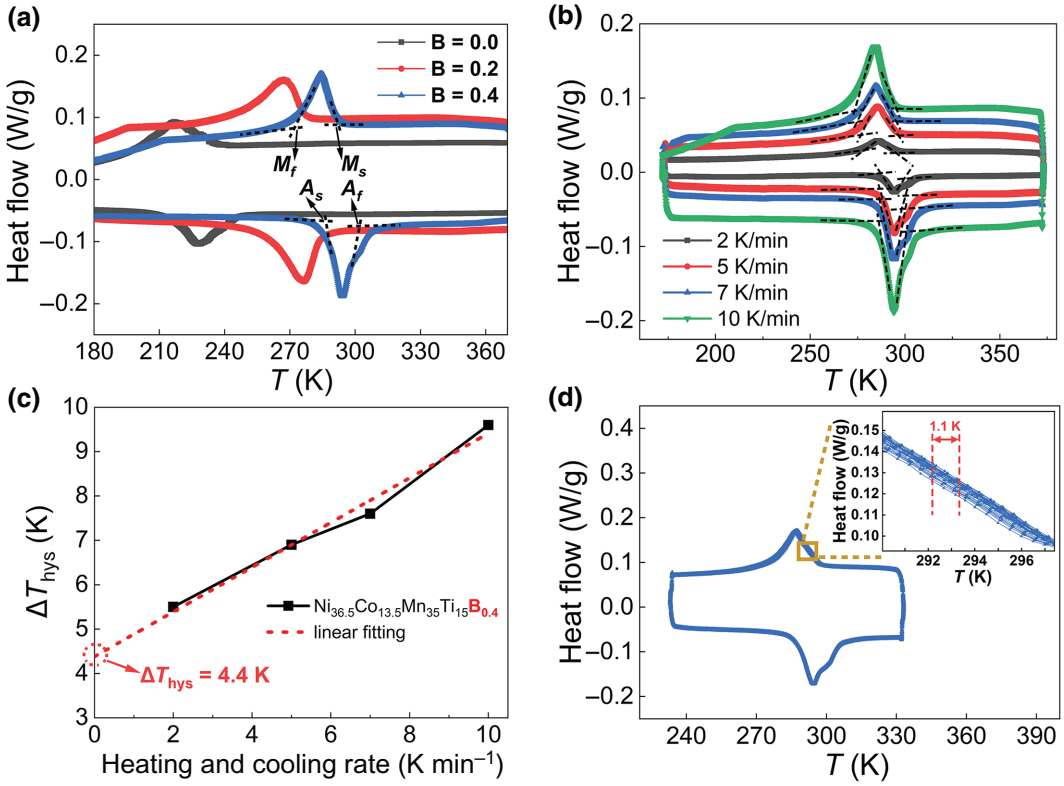

FIG. 1. (a) DSC curves of $Ni_{36.5}Co_{13.5}Mn_{35}Ti_{15}B_x$ ($x = 0.0$, 0.2, 0.4) for heating and cooling at a rate of 10 K/min. (b) DSC curves of $Ni_{36.5}Co_{13.5}Mn_{35}Ti_{15}B_{0.4}$ at different heating and cooling rates. (c) Linear fitting of the ΔT_{hys} obtained at different sweep rates for $Ni_{36.5}Co_{13.5}Mn_{35}Ti_{15}B_{0.4}$. (d) DSC curves and characteristic transformation temperatures in 35 subsequent thermal cycles for $Ni_{36.5}Co_{13.5}Mn_{35}Ti_{15}B_{0.4}$. The inset presents an enlarged part of the curves.

and valence electron concentration (e/a) are summarized in Table I. The thermal hysteresis is defined as $\Delta T_{hys} = (A_s + A_f - M_s - M_f)/2$, and the entropy change as $\Delta S_{tr} = \int_{A_s}^{A_f} \frac{1}{T}(Q - Q_{base})\left(\frac{\partial T}{\partial t}\right)^{-1} dT$, where Q is the heat flow and Q_{base} the baseline for the heat flow [41,42]. With increasing B doping ΔS_{tr} increases from 29.22 to 35.82 J kg^{-1} K^{-1} (18% increment) for a B doping (x) from 0 to 0.4 at. %. This could indicate that the magnetic entropy change ΔS_m also has the potential to increase with B doping as ΔS_{tr} is mainly attributed to the configuration entropy from structural and magnetic contributions [4]. From Table I it is observed that ΔT_{hys} decreases continuously from 13.0 K ($x = 0.0$) to 9.6 K ($x = 0.4$) for an increasing B-doping content. For comparison, the ΔT_{hys} value extracted from SQUID measurement is found to demonstrate a similar reduction from 9.7 K ($x = 0.0$) to 6.8 K ($x = 0.4$). The lower ΔT_{hys} values should be ascribed to the slower heating and cooling rates for the SQUID (2 K/min) in comparison to the DSC (10 K/min) measurements.

As shown in Fig. 1(b), the sweeping rate can affect the determination of ΔT_{hys}. At different DSC scanning rates (10, 7, 5, 2 K/min) the thermal hysteresis of the $Ni_{36.5}Co_{13.5}Mn_{35}Ti_{15}B_{0.4}$ alloy is found to grow at higher sweeping rates, which is caused by thermal lag problems during the measurement. The intrinsic value of ΔT_{hys} for the $Ni_{36.5}Co_{13.5}Mn_{35}Ti_{15}B_{0.4}$ alloy is identified as 4.4 K by extrapolating the results at different sweeping rates towards zero, as demonstrated in Fig. 1(c). This low value for ΔT_{hys} for B-doped Ni-Co-Mn-Ti-based alloys is comparable to the best Ni-Mn-X (X = In, Sb, Sn)-based magnetic Heusler alloys [42,43] and is superior to the previously reported all-d-metal Ni-Co-Mn-Ti-based compounds synthesized and optimized by appropriate heat treatment [20] or rapid-solidification [19] techniques. The general nonlinear theory of martensite (GNLTM) is successfully proposed to explain the relationship of ΔT_{hys} and the interfacial compatibility between the austenite and martensite lattices [44,45]. The interfacial lattice properties of these two phases are related to a 3×3 transformation stretch matrix $\mathbf{U}$, as described below:

$$\mathbf{U} = \begin{bmatrix} \tau & \sigma & 0 \\ \sigma & \rho & 0 \\ 0 & 0 & \delta \end{bmatrix}, \tag{2}$$

where the controlling parameters of the interfacial lattice mismatch are τ, ρ, σ, and δ, which can be derived from the

TABLE I. Characteristic temperatures A_s, A_f, M_s, M_f for starting and finishing points of forward martensitic (M) and reverse austenitic (A) transformations, entropy change of the transformation ΔS_{tr}, thermal hysteresis ΔT_{hys} and e/a for the $Ni_{36.5}Co_{13.5}Mn_{35}Ti_{15}B_x$ ($x = 0.0$, 0.2, 0.4) alloys.

	$A_s{}^{DSC}$ (K)	$A_f{}^{DSC}$ (K)	$M_s{}^{DSC}$ (K)	$M_f{}^{DSC}$ (K)	$\Delta T_{hys}{}^{DSC}$ (K)	$\Delta T_{hys}{}^{SQUID}$ (K)	e/a	ΔS_{tr} (J kg^{-1} K^{-1})
$x = 0.0$	217.0	243.1	239.4	194.8	13.0	9.7	7.915	29.22
$x = 0.2$	259.8	285.1	278.2	244.3	11.2	8.8	7.921	35.58
$x = 0.4$	285.6	300.5	292.7	274.1	9.6	6.8	7.927	35.82

experimental lattice parameters. Note that the above matrix **U** depends on the symmetry of martensite. The modulated monoclinic structure of martensite can be found in Fig. S1 and Table S1 (Supplemental Material [46]). The calculated middle eigenvalue (λ_2) of this matrix **U** for the $x = 0.4$ sample is 0.9913 in comparison to 0.9812 for the undoped sample, which indicates a good geometric compatibility condition. A low value ΔT_{hys} is correlated with a reduced additional free energy to overcome both the stored elastic energy and interfacial energy due to the incompatibility between austenite and martensite (as reflected by a λ_2 close to 1). As these compounds hold a good geometric compatibility for the austenite and the martensite at the phase transition, they are expected to show a longer fatigue life, consistent with our cycled DSC results (only 1.1-K temperature shift after 35 cycles), as shown in Fig. 1(d).

To investigate the influence of B doping on the magnetic properties of Ni-Co-Mn-Ti-based Heusler alloys, Fig. 2(a) and its inset show the temperature-dependent magnetization (M-T) curves for the $Ni_{36.5}Co_{13.5}Mn_{35}Ti_{15}B_x$ ($x = 0.0$, 0.2, 0.4) alloys measured during cooling and heating in magnetic field of 1 T (main panel) and 0.01 T (inset). Interestingly, the structure transition temperatures (T_{tr}) of the martensitic transformation shows a clear increase with B doping. Similarly, the Curie temperatures (T_C) for the ferromagnetic (FM) to paramagnetic (PM) transition present a remarkable increase from 265 K ($x = 0.0$) to 352 ($x = 0.2$) and 361 K ($x = 0.4$). It is well known that for Ni-Mn-based Heusler alloys T_{tr} illustrates a proportional relationship with e/a [47]. As present in Table I, with B ($2s^2 2p^1$) doping the increase in e/a results in the positive shift of T_{tr}. The increase in T_C could, however, reflect an enhanced magnetic exchange interaction among the magnetic atoms. Compared with the undoped sample, the magnetization shows a significant enhancement from 64.4 A m^2 kg^{-1} ($x = 0.0$) to 90.2 A m^2 kg^{-1} ($x = 0.2$) and 82.9 A m^2 kg^{-1} ($x = 0.4$), which demonstrates that interstitial B doping can enhance the magnetic moments and further strengthen the alignment of ferromagnetic spins, and thereby shows a similar effect as substitutional Co doping (the so-called "FM activation effect") [15,48]. The Clausius-Clapeyron relation $dT_{tr}/d(\mu_0 H) = -\Delta M/\Delta S_{tr}$, relates the jump in the magnetization ΔM and the entropy change ΔS_{tr} to the field dependence of the transition. The derived values of $dT_{tr}/d(\mu_0 H)$ at 1 T are 2.2 K/T ($x = 0.0$), 2.5 K/T ($x = 0.2$), 2.3 K/T ($x = 0.4$). As illustrated in Fig. 2(b), for the $Ni_{36.5}Co_{13.5}Mn_{35}Ti_{15}B_{0.4}$ alloy it is found that ΔM can reach 87.9 (5 T) and 93.3 (7 T) A m^2 kg^{-1}. The temperature difference between $A_s = 268.4$ K (5 T) and $M_s = 288.4$ K (0.05 T) is about 20 K, which suggests a substantial reversibility of the magnetic field-induced transformation [49].

Gottschall and coworkers reported that the minor loop method can further minimize the ΔT_{hys} [50]. In Fig. 2(c) scanning with major loops (100 to 370 K) is compared with scanning with minor loops (210 to 315 K). The reduced ΔT_{hys} of 4.2 K for the minor loop (in comparison to the value of 6.5 K for the major loop) can be ascribed to the fact that less nucleation is required for an incomplete martensitic transformation. As shown in Fig. 2(d), the maximum ΔS_m of the parent $Ni_{36.5}Co_{13.5}Mn_{35}Ti_{15}$ alloy can only attain 3.8 and 9.7 J kg^{-1} K^{-1} for a $\Delta\mu_0 H$ of 2 and 5 T, respectively. These relatively low values originate from the relative low magnetization and sluggish magnetostructural phase transition. After B doping the transition sharpens and ΔM increases, resulting in an improvement of ΔS_m in comparison to the undoped sample ($x = 0$).

Figure 3(a) presents the calculated ΔS_m as a function of temperature in the vicinity of the martensitic transition. Here, the $Ni_{36.5}Co_{13.5}Mn_{35}Ti_{15}B_{0.4}$ alloy shows the largest ΔS_m peak at 24.3 J kg^{-1} K^{-1} for $\Delta\mu_0 H = 5$ T (for heating), and even reaches 30.2 J kg^{-1} K^{-1} for $\Delta\mu_0 H = 7$ T (for heating). Compared with the undoped compound ($x = 0.0$), the maximum value of ΔS_m of the doped $Ni_{36.5}Co_{13.5}Mn_{35}Ti_{15}B_{0.4}$ sample shows a remarkable improvement by a factor 2.5 from 9.7 to 24.3 J kg^{-1} K^{-1} for a field change of $\Delta\mu_0 H = 5$ T. For the application scenarios the reversible ΔS_m should be considered. As shown in Fig. 3(b), the isothermal magnetic field-cycled M-H loops (first cycle is indicated by the solid symbols and the second cycle by the open symbols) are measured in the temperature range from 268 to 288 K. It is found that the M-H curves do not overlap with each other during the first increase and the second decrease of the magnetic field cycles. This could result from the presence of some residual austenite that does not contribute to the transformation of the field cycles. The so-called transformation fraction (TF_MB) method can be applied

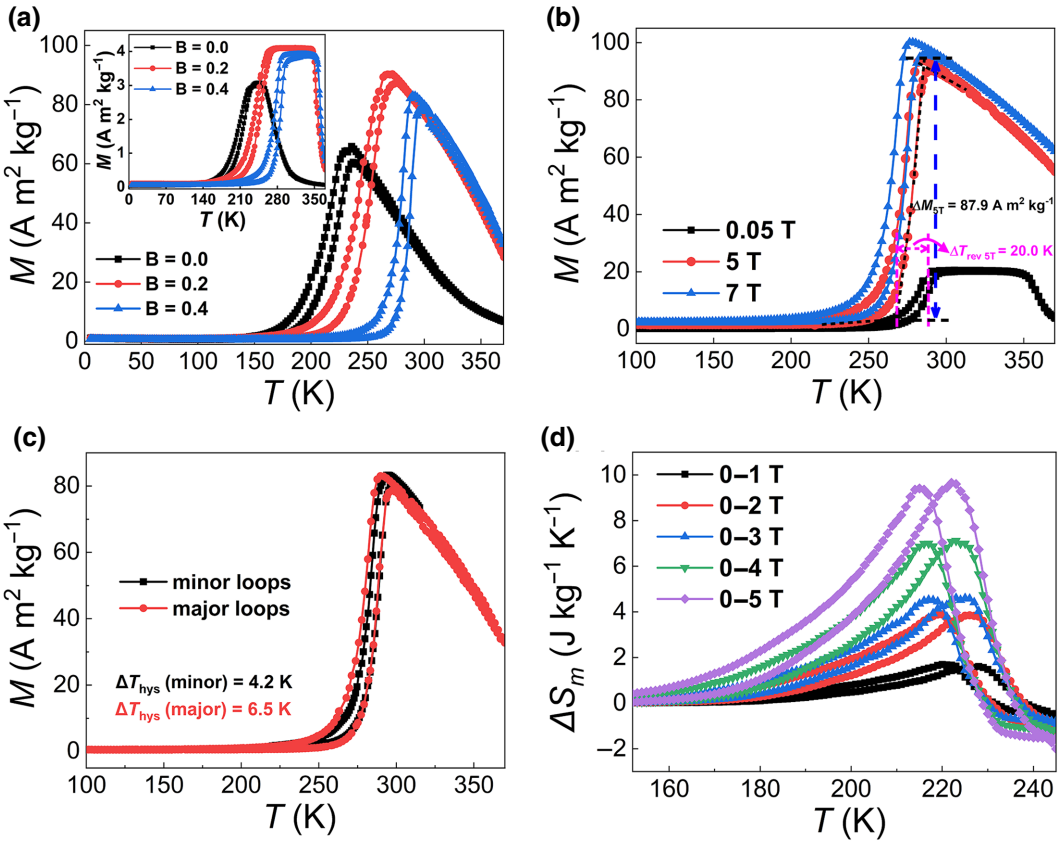

FIG. 2. (a) M-T curves measured in 1 T for $Ni_{36.5}Co_{13.5}Mn_{35}Ti_{15}B_x$ ($x = 0.0$, 0.2, 0.4) alloys. The inset corresponds to the M-T curves at 0.01 T. (b) M-T curves for $Ni_{36.5}Co_{13.5}Mn_{35}Ti_{15}B_{0.4}$ in applied magnetic fields of 0.05, 5, and 7 T. The determination of ΔM is illustrated in the figure. (c) M-T curves of $Ni_{36.5}Co_{13.5}Mn_{35}Ti_{15}B_{0.4}$ for minor and major hysteresis loops in different temperature ranges at 1 T. (d) ΔS_m of $Ni_{36.5}Co_{13.5}Mn_{35}Ti_{15}$ as a function of temperature for both heating and cooling, determined in magnetic fields ($\Delta\mu_0 H$) ranging from 1 to 5 T.

on the basis of the assumption that the total magnetization originates from the ferromagnetic austenite phase fraction [49,51]. Consequently, the reversible ΔS_m ($\Delta S_m{}^{\mathrm{rev}}$) can then be estimated by combining Eqs. (3) and (4):

$$f_{\mathrm{aus}}(T,H) = \frac{M(H) - M_m(H)}{M_a(H) - M_m(H)}, \tag{3}$$

$$\Delta S_m^{\mathrm{rev}} = \Delta f \times \Delta S_{\mathrm{tr}} = (f(T,H_f) - f(T,H_i)) \times \Delta S_{\mathrm{tr}}, \tag{4}$$

where $f_{\mathrm{aus}}(T,H)$ is the austenite fraction at certain temperature and field, ΔS_{tr} donates the entropy change of the transformation (see Table I), Δf is the transformed austenite fraction, $M(H)$ is the measured magnetization, and $M_m(H)$ is the magnetization of pure martensite [see the extrapolated black dotted lines in Fig. 3(b)]. Correspondingly, $M_a(H)$ is the magnetization of pure austenite. Note that the M-H curve at 300 K is chosen as the benchmark for pure austenite to avoid an underestimation of the austenite fraction at low fields, as shown in Fig. S2(a) (Supplemental Material [46]). Consequently, for the $Ni_{36.5}Co_{13.5}Mn_{35}Ti_{15}B_{0.4}$ alloy the f_{aus} of the first and second field cycle at different constant temperatures are derived, as in Figs. 3(c) and 3(d).

Nevertheless, even though B doping significantly improve ΔS_m as mentioned above, it is worthwhile to note that its low field sensitivity of transition temperature $dT_{\mathrm{tr}}/d(\mu_0 H)$, which ranges from 1 to 3 K/T for this all-d-metal Ni-Co-Mn-Ti Heusler alloy system, could be detrimental to low-field (less than 2 T) applications [19,20]. In our present study the $Ni_{36.5}Co_{13.5}Mn_{35}Ti_{15}B_{0.4}$ alloy shows a moderate $dT_{\mathrm{tr}}/d(\mu_0 H)$ value of 2.3 K/T. It has been reported that the reversible ΔS_m can roughly be determined by the overlap area of the heating and cooling branches in the ΔS_m-temperature curves [42,52,53]. Due to its low ΔT_{hys}, as shown in Fig. 4(a), the maximum reversible ΔS_m for the $Ni_{36.5}Co_{13.5}Mn_{35}Ti_{15}B_{0.4}$ alloy (see gray area) is estimated at 21.2 and 27.5 J kg^{-1} K^{-1} for a field change of $\Delta\mu_0 H = 5$ and 7 T, respectively. For comparison, in Fig. 4(b) the ΔS_m for first and second field cycles are extracted by applying the TF_MB method. In comparison to the ΔS_m obtained from the

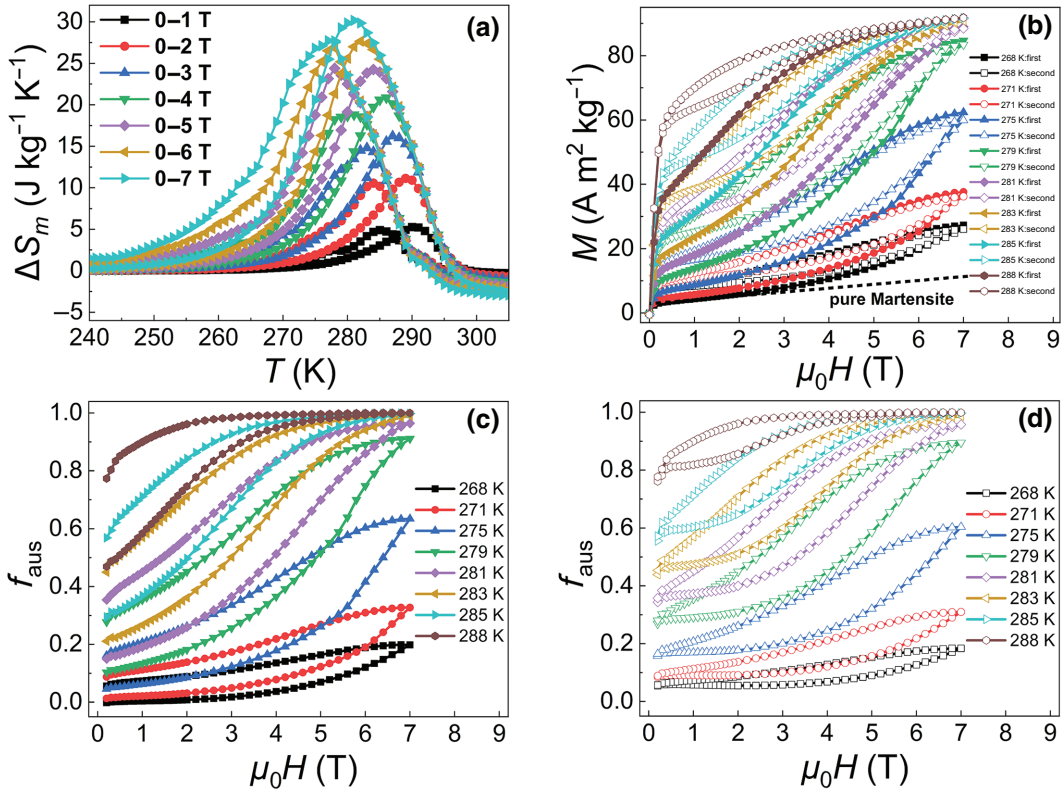

FIG. 3. (a) Magnetic entropy change ΔS_m of the $Ni_{36.5}Co_{13.5}Mn_{35}Ti_{15}B_{0.4}$ alloy as a function of temperature for both heating and cooling determined for magnetic field changes $\Delta\mu_0 H$ ranging from 1 to 7 T. (b) Isothermal M-H curves for the $Ni_{36.5}Co_{13.5}Mn_{35}Ti_{15}B_{0.4}$ alloy measured during the first (solid symbols) and second (open symbols) cycle for increasing and decreasing magnetic fields at different temperatures. The dotted lines denote the extrapolated magnetization for pure martensite. The fraction of austenite f_{aus} for (c) the first field cycle and (d) second cycle at different constant temperatures determined from (b).

Maxwell relation (first cycle), the ΔS_m with $\Delta\mu_0 H = 7$ T obtained by the TF_MB method (first cycle) shows consistent results, while the second cycle ΔS_m (corresponding to the reversible part and indicated by the red dashed line) shows a slightly reduction (22.0 J kg^{-1} K^{-1} at 281 K). The maximum reversible $\Delta S_m{}^{rev}$ value is determined as 18.9 J kg^{-1} K^{-1} at 283 K with $\Delta\mu_0 H = 5$ T as presented in Figs. S2(b)–S2(d) (Supplemental Material [46]), which is competitive with traditional Ni-Mn-based Heusler alloys like $Ni_{49.8}Co_{1.2}Mn_{33.5}In_{15.5}$ (14.6 J kg^{-1} K^{-1}) [54], $Ni_{41}Ti_1Co_9Mn_{39}Sn_{10}$ (18.7 J kg^{-1} K^{-1}) [49], $Ni_{48.1}Co_{2.9}Mn_{35.0}In_{14.0}$ (12.8 J kg^{-1} K^{-1}) [55], $Ni_{43}Co_6Mn_{40}Sn_{11}$ (19.3 J kg^{-1} K^{-1}) [56], $Ni_{46}Co_3Mn_{35}Cu_2In_{14}$ (16.4 J kg^{-1} K^{-1}) [57].

Additionally, we apply calorimetric measurements (in-field DSC) to obtain ΔS_m and ΔT_{ad} for the $Ni_{36.5}Co_{13.5}Mn_{35}Ti_{15}B_{0.4}$ alloy at low applied magnetic fields (up to 1.5 T). As shown in Fig. S3(a) (Supplemental Material [46]), with increasing applied magnetic field the specific heat peak shows a decrease, which is characteristic for an inverse MCE. In Fig. S3(c) (Supplemental Material [46]) the extracted ΔS_m for $\Delta\mu_0 H = 1$ T (5.0 J kg^{-1} K^{-1}) extracted from the in-field DSC is in close agreement with the value obtained from the Maxwell relation (5.2 J kg^{-1} K^{-1}). From Fig. S3(d) the value of ΔT_{ad} can be determined as -1.1 K ($\Delta\mu_0 H = 1$ T) and -1.8 K ($\Delta\mu_0 H = 1.5$ T). As shown in Fig. S4(b) (Supplemental Material [46]) by applying the equation $\Delta T_{ad} = -(T/C_p)\Delta S_m$ values of ΔT_{ad} for different B content samples can be estimated. Compared to the nondoped sample ($x = 0.0$), the $x = 0.4$ sample shows the maximum $|\Delta T_{ad}|$ value for a field change of 5 T, with an increase from 3.2 K ($x = 0.0$) to 7.4 K ($x = 0.4$).

Although a colossal elastocaloric effect [58] and giant barocaloric effect [59] have been achieved by boron doping (substitutional method), the underlying mechanism associated with the doped B atoms was not studied. To further investigate the mechanism responsible for the positive influence of B doping on the MCE in the Ni-Co-Mn-Ti system, it is crucial to understand what lattice site the B occupancies (interstitial or substitutional). For the $(Mn, Fe)_2(P, Si)$-type MCMs both experimental

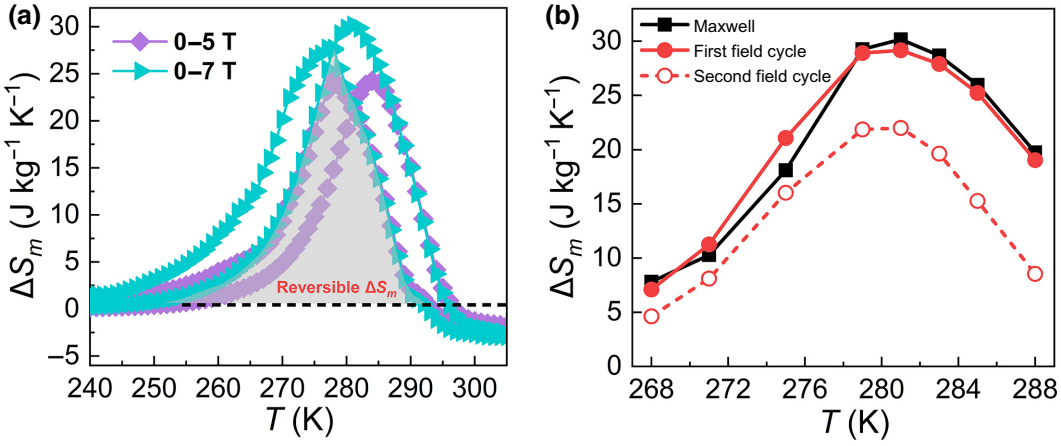

FIG. 4. (a) Magnetic entropy change ΔS_m as a function of temperature for the $Ni_{36.5}Co_{13.5}Mn_{35}Ti_{15}B_{0.4}$ alloy upon heating and cooling in high magnetic field changes of 5 and 7 T. The shaded area corresponds to the reversible ΔS_m. (b) ΔS_m for a magnetic field change of 0–7 T obtained from the Maxwell relation and the TF_MB method during the first and second cycles. In the second cycle ΔS_m is reversible.

and computational studies indicate that light atoms, like B, C, and N, have a distinctly different effect on the MCE for interstitial or substitutional doping [60]. As illustrated in Fig. 5(a), based on the typical $L2_1$ cubic austenite structure for Ni-Mn-based Heusler alloys, the supercell shown in the inset of Fig. 5(a) has been constructed for our B-doped Ni-Co-Mn-Ti system. The formation energies E_f of different site-occupation models are calculated on the basis of *ab initio* first-principles calculations, as shown in Fig. 5(a). Based on $L2_1$ crystal structure, three kinds of interstitial sites are considered [61]: one tetrahedral interstice (labeled as *T*) and two octahedral interstices (labeled as *O*-I and *O*-II). It is found that for our case the B atoms prefer to enter structure at an interstitial site rather than substitutional site. The B atoms are found to preferentially occupy the *O*-I octahedral interstitial site (24*d* site of the *Fm*-3*m* space group). The experimental XRD results shown in Fig. S5(b) (Supplemental Material [46]) also prove that B enters interstitially as the unit cell linearly expands with increasing B content (up to 0.4 at. %). Note that for a B content above 0.4 at. % the doping reaches its limitation (indicated by the yellow area). The corresponding DSC curves and *M*-*T* curves at 0.01 and 1 T are presented in Figs. S6 and S7 (Supplemental Material [46]). An extra Mn_2B impurity phase (space group: *I*4/*mcm*) appeared with a concentration of about 3.3(7) wt % for the $x = 0.8$ sample, as shown in Fig. S8 (Supplemental Material [46]). From the Mn-B binary phase diagram [62] we know Mn_2B is very stable between 600–1120 °C (the annealing temperature is 900 °C). The created impurity phase has a significant influence for the system. For instance, in Fig. S7(b) (Supplemental Material [46]) an obvious decrease in magnetization and transition temperature is observed for the $x = 0.8$ sample as the Mn atoms are mainly responsible for the magnetic moments for Ni-Mn-based magnetic Heusler alloys. The interstitially doped B increases the Mn-Mn distance, which is found to control the size of the magnetic moments [63,64]. B doping will further improve the strong FM ordering based on Mn-Co-Mn configuration ("Co activation effect"). Interestingly, this B improvement of the magnetic moment is also observed computationally. DFT calculations indicate that the magnetic moment increases from 4.62 μ_B/f.u. in the undoped system to 4.75 μ_B/f.u. in the B-doped system (1.6 at. % B).

To further investigate the underlying mechanisms of interstitial B doping on the local electronic environment, the ELF is calculated, providing a visualization of the valence electron pair-repulsion theory. ELF values for the slice along the (110) direction for the undoped and the B-doped Ni-Co-Mn-Ti alloys, are displayed in Figs. 5(b) and 5(c), respectively. It is observed that more localized electrons are concentrated in the surrounding of the B located at the *O*-I interstitial site. To quantitatively study the variation in bonding character between covalent and metallic bonding, line profiles of ELF values between nearest-neighbor atom pairs are illustrated in Figs. 5(d) and 5(e). Note that a higher ELF value means more electron localization. Compared to the undoped system, the most prominent features for the maximum ELF values of the doped system are as follows: an 33.3% increment of Mn-Mn (from 0.12 to 0.16) and an 21.4% increment of Mn-Ni (from 0.14 to 0.17), which suggest a stronger covalent-like bonding between the Mn-Mn and Mn-Ni atoms. In contrast to Ni-Mn-*X* (X = Al, Ga, In, Sn)-based Heusler alloys stabilized by *p*-*d* covalent hybridization, the all-*d*-metal Ni-Co-Mn-Ti-based alloys are essentially associated with *d*-*d* covalent hybridization [15]. Consequently, after B

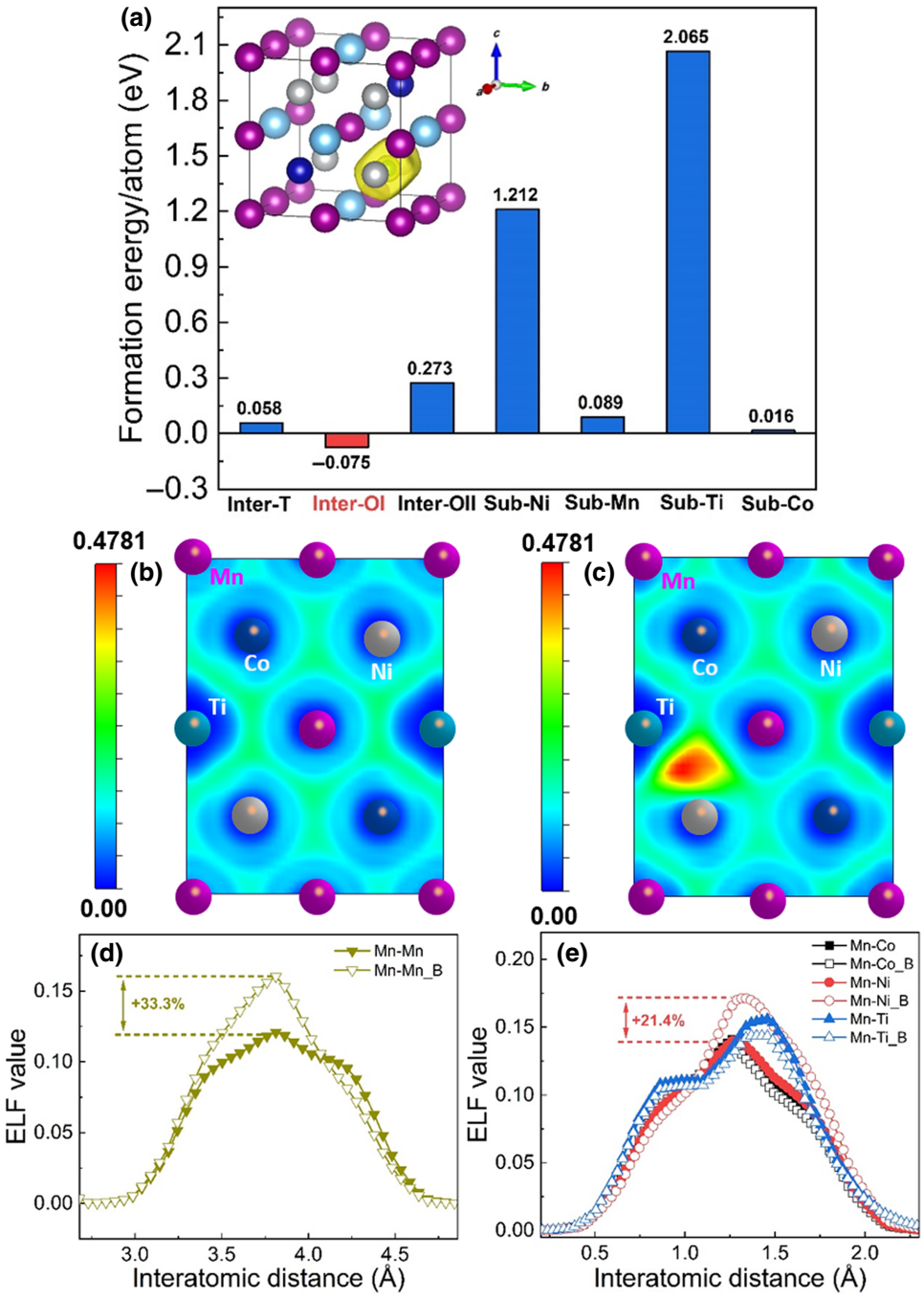

FIG. 5. (a) Formation energy E_f for different site-occupation models for B-doped Ni-Co-Mn-Ti materials. Calculated ELF contour maps sliced along the (110) direction for (b) no dopant and (c) B-doped Ni-Co-Mn-Ti-based alloys. (d) Line profiles of the ELF values between Mn and its nearest Mn atom. (e) Line profiles of the ELF values between Mn and its nearest Co/Ni/Ti neighbors.

doping the coordination electronic environment of Mn-Mn and Mn − Ni will be affected.

IV. CONCLUSIONS

In summary, interstitial B doping is successfully applied for all-*d*-metal $Ni_{36.5}Co_{13.5}Mn_{35}Ti_{15}B_x$ ($x = 0$, 0.2, 0.4, 0.6, and 0.8) magnetic Heusler alloys. It is demonstrated that doping with the light element B provides an efficient method to positively influence the magnetocaloric properties of the system. B doping significantly reduces the thermal hysteresis ΔT_{hys}, which could be ascribed to the good geometric compatibility between martensite and austenite. B doping also significantly improves ΔS_m by strengthening the FOMT. The low value for ΔT_{hys} obtained by B doping directly causes an excellent reversibility performance for the $Ni_{36.5}Co_{13.5}Mn_{35}Ti_{15}B_{0.4}$ alloy with a maximum ΔS_m^{rev} that can reach 18.9 (283 K) and 22.0 J kg^{-1} K^{-1} (281 K) for a field change $\Delta\mu_0 H$ of 5 and 7 T, respectively. This in combination with the favorable mechanical properties makes it a competitive candidate compared with traditional Ni-Mn-*X*-based Heusler

alloys (X = Ga, In, Sn, Sb). The experimentally observed enhanced magnetic moments are in line with DFT calculations. Combining XRD and first-principles calculations, the site preference for doping of B atoms is identified as the *O*-I octahedral interstitial site. Furthermore, ELF calculations illustrate the changes in electron localization before and after B doping. Our studies pave the way for further optimization of the GMCE, and provide insights in this all-*d*-metal Ni-Co-Mn-Ti magnetic Heusler alloy system.

ACKNOWLEDGMENTS

The authors thank Anton Lefering, Bert Zwart, Robert Dankelman, and Michel Steenvoorden for their technical assistance. This work is financially supported by NWO in the domain of the Applied and Engineering Sciences (AES) program. Fengqi Zhang gratefully acknowledges financial support from the China Scholarship Council.

[1] X. Moya and N. D. Mathur, Caloric materials for cooling and heating, Science **370**, 797 (2020).

[2] H. Johra, K. Filonenko, P. Heiselberg, C. Veje, S. Dall'Olio, K. Engelbrecht, and C. Bahl, Integration of a magnetocaloric heat pump in an energy flexible residential building, Renewable Energy **136**, 115 (2019).

[3] D. Dzekan, A. Waske, K. Nielsch, and S. Fahler, Efficient and affordable thermomagnetic materials for harvesting low grade waste heat, Appl. Mater. **9**, 011105 (2021).

[4] M. E. Gruner, W. Keune, B. Roldan Cuenya, C. Weis, J. Landers, S. I. Makarov, D. Klar, M. Y. Hu, E. E. Alp, J. Zhao, M. Krautz, O. Gutfleisch, and H. Wende, Element-Resolved Thermodynamics of Magnetocaloric $LaFe_{13-x}Si_x$, Phys. Rev. Lett. **114**, 057202 (2015).

[5] O. Tegus, E. Brück, K. H. J. Buschow, and F. R. de Boer, Transition-metal-based magnetic refrigerants for room-temperature applications, Nature **415**, 150 (2002).

[6] F. X. Hu, B. G. Shen, J. R. Sun, Z. H. Cheng, G. H. Rao, and X. X. Zhang, Influence of negative lattice expansion and metamagnetic transition on magnetic entropy change in the compound $LaFe_{11.4}Si_{1.6}$, Appl. Phys. Lett. **78**, 3675 (2001).

[7] E. Stern-Taulats, A. Planes, P. Lloveras, M. Barrio, J. L. Tamarit, S. Pramanick, S. Majumdar, C. Frontera, and L. Manosa, Barocaloric and magnetocaloric effects in $Fe_{49}Rh_{51}$, Phys. Rev. B **89**, 214105 (2014).

[8] F. Guillou, A. K. Pathak, D. Paudyal, Y. Mudryk, F. Wilhelm, A. Rogalev, and V. K. Pecharsky, Non-hysteretic first-order phase transition with large latent heat and giant low-field magnetocaloric effect, Nat. Commun. **9**, 2925 (2018).

[9] V. K. Pecharsky and K. A. Gschneidner, Giant Magnetocaloric Effect in $Gd_5(Si_2Ge_2)$, Phys. Rev. Lett. **78**, 4494 (1997).

[10] A. Planes, L. Manosa, and M. Acet, Magnetocaloric effect and its relation to shape-memory properties in ferromagnetic Heusler alloys, J. Phys.: Condens. Matter **21**, 233201 (2009).

[11] E. K. Liu, W. H. Wang, L. Feng, W. Zhu, G. J. Li, J. L. Chen, H. W. Zhang, G. H. Wu, C. B. Jiang, H. B. Xu, and F. R. de Boer, Stable magnetostructural coupling with tunable magnetoresponsive effects in hexagonal ferromagnets, Nat. Commun. **3**, 873 (2012).

[12] J. Liu, Y. Y. Gong, Y. R. You, X. M. You, B. W. Huang, X. F. Miao, G. Z. Xu, F. Xu, and E. Brück, Giant reversible magnetocaloric effect in MnNiGe-based materials: Minimizing thermal hysteresis via crystallographic compatibility modulation, Acta. Mater. **174**, 450 (2019).

[13] S. Pandey, A. Quetz, A. Aryal, I. Dubenko, D. Mazumdar, S. Stadler, and N. Ali, Large inverse magnetocaloric effects and giant magnetoresistance in Ni-Mn-Cr-Sn Heusler alloys, Magnetochemistry **3**, 3 (2017).

[14] J. Sharma and K. G. Suresh, Observation of giant exchange bias in bulk $Mn_{50}Ni_{42}Sn_8$ Heusler alloy, Appl. Phys. Lett. **106**, 072405 (2015).

[15] Z. Y. Wei, E. K. Liu, J. H. Chen, Y. Li, G. D. Liu, H. Z. Luo, X. K. Xi, H. W. Zhang, W. H. Wang, and G. H. Wu, Realization of multifunctional shape-memory ferromagnets in all-*d*-metal Heusler phases, Appl. Phys. Lett. **107**, 022406 (2015).

[16] V. G. de Paula and M. S. Reis, All-*d*-metal *full* Heusler alloys: A novel class of functional materials, Chem. Mater. **33**, 5483 (2021).

[17] Z. N. Ni, X. M. Guo, X. T. Liu, Y. Y. Jiao, F. B. Meng, and H. Z. Luo, Understanding the magnetic structural transition in all-d-metal Heusler alloy $Mn_2Ni_{1.25}Co_{0.25}Ti_{0.5}$, J. Alloys Compd. **775**, 427 (2019).

[18] Z. Q. Guan, J. Bai, J. L. Gu, X. Z. Liang, D. Liu, X. J. Jiang, R. K. Huang, Y. D. Zhang, L. D. Esling, X. Zhao, and L. Zuo, First-principles investigation of B2 partial disordered structure, martensitic transformation, elastic and magnetic properties of all-d-metal Ni-Mn-Ti Heusler alloys, J. Mater. Sci. Technol. **68**, 103 (2021).

[19] H. N. Bez, A. K. Pathak, A. Biswas, N. Zarkevich, V. Balema, Y. Mudryk, D. D. Johnson, and V. K. Pecharsky, Giant enhancement of the magnetocaloric response in Ni-Co-Mn-Ti by rapid solidification, Acta. Mater. **173**, 225 (2019).

[20] A. Taubel, B. Beckmann, L. Pfeuffer, N. Fortunato, F. Scheibel, S. Ener, T. Gottschall, K. P. Skokov, H. R. Zhang, and O. Gutfleisch, Tailoring magnetocaloric effect in all-*d*-metal Ni-Co-Mn-Ti Heusler alloys: A combined experimental and theoretical study, Acta. Mater. **201**, 425 (2020).

[21] T. Gottschall, E. Bykov, A. Gracia-Condal, B. Beckmann, A. Taubel, L. Pfeuffer, O. Gutfleisch, L. I. Manosa, A. Planes, Y. Skourski, and J. Wosnitza, Advanced characterization of multicaloric materials in pulsed magnetic fields, J. Appl. Phys. **127**, 185107 (2020).

[22] Y. Li, L. Qin, S. Y. Huang, and L. W. Li, Enhanced magnetocaloric performances and tunable martensitic transformation in $Ni_{35}Co_{15}Mn_{35-x}Fe_xTi_{15}$ all-d-metal Heusler alloys by chemical and physical pressures, Sci. China. Mater. **65**, 486 (2021).

[23] Z. Q. Guan, X. J. Jiang, J. L. Gu, J. Bai, X. Z. Liang, H. L. Yan, Y. D. Zhang, L. D. Esling, X. Zhao, and L. Zuo, Large magnetocaloric effect and excellent mechanical properties near room temperature in Ni-Co-Mn-Ti

non-textured polycrystalline alloys, Appl. Phys. Lett. **119**, 051904 (2021).

[24] F. Guillou, G. Porcari, H. Yibole, N. van Dijk, and E. Brück, Taming the first-order transition in giant magnetocaloric materials, Adv. Mater. **26**, 2671 (2014).

[25] N. V. Thang, X. F. Miao, N. H. van Dijk, and E. Brück, Structural and magnetocaloric properties of $(Mn, Fe)_2(P, Si)$ materials with added nitrogen, J. Alloys Compd. **670**, 123 (2016).

[26] H. Z. Luo, F. B. Meng, Q. X. Jiang, H. Y. Liu, E. K. Liu, G. H. Wu, and Y. X. Wang, Effect of boron on the martensitic transformation and magnetic properties of $Ni_{50}Mn_{36.5}Sb_{13.5-x}B_x$ alloys, Scr. Mater. **63**, 569 (2010).

[27] Y. Zhang, J. Liu, Q. Zheng, J. Zhang, W. X. Xia, J. Du, and A. R. Yan, Large magnetic entropy change and enhanced mechanical properties of Ni-Mn-Sn-C alloys, Scr. Mater. **75**, 26 (2014).

[28] S. Pandey, A. Quetz, I. D. Rodionov, A. Aryal, M. I. Blinov, I. S. Titov, V. N. Prudnikov, A. B. Granovsky, I. Dubenko, S. Stadler, and N. Ali, Magnetic, transport, and magnetocaloric properties of boron doped Ni-Mn-In alloys, J. Appl. Phys. **117**, 183905 (2015).

[29] S. Kavita, V. V. Ramakrishna, P. Yadav, S. Kethavath, N. P. Lalla, T. Thomas, P. Bhatt, and R. Gopalan, Enhancement of martensite transition temperature and inverse magnetocaloric effect in $Ni_{43}Mn_{47}Sn_{11}$ alloy with B doping, J. Alloys Compd. **795**, 519 (2019).

[30] G. Porcari, F. Cugini, S. Fabbrici, C. Pernechele, F. Albertini, M. Buzzi, M. Mangia, and M. Solzi, Convergence of direct and indirect methods in the magnetocaloric study of first order transformations: The case of Ni-Co-Mn-Ga Heusler alloys, Phys. Rev. B **86**, 104432 (2012).

[31] G. Porcari, M. Buzzi, F. Cugini, R. Pellicelli, C. Pernechele, L. Caron, E. Brück, and M. Solzi, Direct magnetocaloric characterization and simulation of thermomagnetic cycles, Rev. Sci. Instrum. **84**, 073907 (2013).

[32] H. M. Rietveld, A profile refinement method for nuclear and magnetic structures, J. Appl. Crystallogr. **2**, 65 (1969).

[33] L. Caron, Z. Q. Ou, T. T. Nguyen, D. T. C. Thanh, O. Tegus, and E. Brück, On the determination of the magnetic entropy change in materials with first-order transitions, J. Magn. Magn. Mater. **321**, 3559 (2009).

[34] G. Kresse and J. Hafner, Ab initio molecular dynamics for liquid metals, Phys. Rev. B **47**, 558 (1993).

[35] G. Kresse and J. Furthmuller, Efficiency of ab-initio total energy calculations for metals and semiconductors using a plane-wave basis set, Comput. Mater. Sci. **6**, 15 (1996).

[36] P. E. Blochl, Projector augmented-wave method, Phys. Rev. B **50**, 17953 (1994).

[37] G. Kresse and D. Joubert, From ultrasoft pseudopotentials to the projector augmented-wave method, Phys. Rev. B **59**, 1758 (1999).

[38] J. P. Perdew, K. Burke, and M. Ernzerhof, Generalized Gradient Approximation Made Simple, Phys. Rev. Lett. **77**, 3865 (1996).

[39] M. Methfessel and A. T. Paxton, High-precision sampling for Brillouin-Zone integration in metals, Phys. Rev. B **40**, 3616 (1989).

[40] B. Silvi and A. Savin, Classification of chemical-bonds based on topological analysis of electron localization functions, Nature **371**, 683 (1994).

[41] B. D. Ingale, Y. K. Kuo, and S. Ram, Phase transformation, microstructure and magnetocaloric properties in polycrystalline bulk $Ni_{50}Mn_{50-z}Sn_z$ alloys, IEEE. Trans. Magn. **47**, 3395 (2011).

[42] J. Liu, X. M. You, B. W. Huang, I. Batashev, M. Maschek, Y. Y. Gong, X. F. Miao, F. Xu, N. van Dijk, and E. Brück, Reversible low-field magnetocaloric effect in Ni-Mn-In-based Heusler alloys, Phys. Rev. Mater. **3**, 084409 (2019).

[43] A. A. Mendonca, L. Ghivelder, P. L. Bernardo, H. L. Gu, R. D. James, L. F. Cohen, and A. M. Gomes, Experimentally correlating thermal hysteresis and phase compatibility in multifunctional Hensler alloys, Phys. Rev. Mater. **4**, 114403 (2020).

[44] J. Cui, Y. S. Chu, O. O. Famodu, Y. Furuya, J. Hattrick-Simpers, R. D. James, A. Ludwig, S. Thienhaus, M. Wuttig, Z. Y. Zhang, and I. Takeuchi, Combinatorial search of thermoelastic shape-memory alloys with extremely small hysteresis width, Nat. Mater. **5**, 286 (2006).

[45] Y. T. Song, X. Chen, V. Dabade, T. W. Shield, and R. D. James, Enhanced reversibility and unusual microstructure of a phase-transforming material, Nature **502**, 85 (2013).

[46] See Supplemental Material at http://link.aps.org/supplemental/10.1103/PhysRevApplied.17.054032. Figure S1 shows the refined powder XRD patterns for the $x = 0.0$ (204 K) and $x = 0.4$ (room temperature) alloys with a two-phase coexistence of the modulated monoclinic martensite and cubic austenite. Figure S2 presents (a) M-H curves of the austenite phase at different temperatures for the $x = 0.4$ alloy. The M-H curve at 300 K is chosen as the benchmark for the pure austenite state when the "TF_MB" method is applied. (c), (d) M-H curves in magnetic fields up to 5 T for different cycles and corresponding austenite fractions. Figure S3 shows the calorimetric ΔS_m and ΔT_{ad} estimation. Figure S4 shows the ΔS_m and ΔT_{ad} changes as a function of B content. Figure S5 presents powder XRD patterns of high-temperature pure austenite and lattice parameters. Figures S6 and S7 show DSC and M-T curves for different B-doped samples, respectively. Figure S8 shows refined powder XRD patterns of pure austenite for (a) $x = 0.4$ (393 K) and (b) $x = 0.8$ (room temperature) alloys. Tables S1 and S2 show lattice parameters of martensite and austenite, respectively.

[47] M. Khan, J. Jung, S. S. Stoyko, A. Mar, A. Quetz, T. Samanta, I. Dubenko, N. Ali, S. Stadler, and K. H. Chow, The role of Ni-Mn hybridization on the martensitic phase transitions in Mn-rich Heusler alloys, Appl. Phys. Lett. **100**, 172403 (2012).

[48] Z. Y. Wei, E. K. Liu, Y. Li, X. L. Han, Z. W. Du, H. Z. Luo, G. D. Liu, X. K. Xi, H. W. Zhang, W. H. Wang, and G. H. Wu, Magnetostructural martensitic transformations with large volume changes and magneto-strains in all-d-metal Heusler alloys, Appl. Phys. Lett. **109**, 071904 (2016).

[49] Y. H. Qu, D. Y. Cong, X. M. Sun, Z. H. Nie, W. Y. Gui, R. G. Li, Y. Ren, and Y. D. Wang, Giant and reversible room-temperature magnetocaloric effect in

Ti-doped Ni-Co-Mn-Sn magnetic shape memory alloys, Acta. Mater. **134**, 236 (2017).

[50] T. Gottschall, K. P. Skokov, B. Frincu, and O. Gutfleisch, Large reversible magnetocaloric effect in Ni-Mn-In-Co, Appl. Phys. Lett. **106**, 021901 (2015).

[51] K. Xu, Z. Li, Y. L. Zhang, and C. Jing, An indirect approach based on Clausius-Clapeyron equation to determine entropy change for the first-order magnetocaloric materials, Phys. Lett. A **379**, 3149 (2015).

[52] B. Kaeswurm, V. Franco, K. P. Skokov, and O. Gutfleisch, Assessment of the magnetocaloric effect in La, Pr(Fe, Si) under cycling, J. Magn. Magn. Mater. **406**, 259 (2016).

[53] M. Fries, L. Pfeuffer, E. Bruder, T. Gottschall, S. Ener, L. V. S. Diop, T. Grob, K. P. Skokov, and O. Gutfleisch, Microstructural and magnetic properties of Mn-Fe-P-Si (Fe_2P-type) magnetocaloric compounds, Acta. Mater. **132**, 222 (2017).

[54] L. Huang, D. Y. Cong, L. Ma, Z. H. Nie, Z. L. Wang, H. L. Suo, Y. Ren, and Y. D. Wang, Large reversible magnetocaloric effect in a Ni-Co-Mn-In magnetic shape memory alloy, Appl. Phys. Lett. **108**, 032405 (2016).

[55] Y. H. Qu, D. Y. Cong, Z. Chen, W. Y. Gui, X. M. Sun, S. H. Li, L. Ma, and Y. D. Wang, Large and reversible inverse magnetocaloric effect in $Ni_{48.1}Co_{2.9}Mn_{35.0}In_{14.0}$ metamagnetic shape memory microwire, Appl. Phys. Lett. **111**, 192412 (2017).

[56] Y. H. Qu, D. Y. Cong, S. H. Li, W. Y. Gui, Z. H. Nie, M. H. Zhang, Y. Ren, and Y. D. Wang, Simultaneously achieved large reversible elastocaloric and magnetocaloric effects and their coupling in a magnetic shape memory alloy, Acta. Mater. **151**, 41 (2018).

[57] Z. B. Li, J. J. Yang, D. Li, Z. Z. Li, B. Yang, H. L. Yan, C. F. Sanchez-Valdes, J. L. S. Llamazares, Y. D. Zhang, C. Esling, X. Zhao, and L. Zuo, Tuning the reversible magnetocaloric effect in Ni-Mn-In-based alloys through Co and Cu co-doping, Adv. Electron. Mater. **5**, 1800845 (2019).

[58] D. Y. Cong, W. X. Xiong, A. Planes, Y. Ren, L. Manosa, P. Y. Cao, Z. H. Nie, X. M. Sun, Z. Yang, X. F. Hong, and Y. D. Wang, Colossal Elastocaloric Effect in Ferroelastic Ni-Mn-Ti Alloys, Phys. Rev. Lett. **122**, 255703 (2019).

[59] A. Aznar, A. Gràcia-Condal, A. Planes, P. Lloveras, M. Barrio, J. L. Tamarit, W. X. Xiong, D. Y. Cong, C. Popescu, and L. Mañosa, Giant barocaloric effect in all-*d*-metal Heusler shape memory alloys, Phys. Rev. Mater. **3**, 044406 (2019).

[60] X. F. Miao, S. Y. Hu, F. Xu, and E. Brück, Overview of magnetoelastic coupling in $(Mn, Fe)_2(P, Si)$-type magnetocaloric materials, Rare Met. **37**, 723 (2018).

[61] H. L. Yan, H. X. Liu, Y. Zhao, N. Jia, J. Bai, B. Yang, Z. B. Li, Y. D. Zhang, C. Esling, X. Zhao, and L. Zuo, Impact of B alloying on ductility and phase transition in the Ni-Mn-based magnetic shape memory alloys: Insights from first-principles calculation, J. Mater. Sci. Technol. **74**, 27 (2021).

[62] P. K. Liao and K. E. Spear, The B−Mn (Boron-Manganese) system, Bull. Alloy Phase Diagrams **7**, 543 (1986).

[63] E. C. Passamani, F. Xavier, E. Favre-Nicolin, C. Larica, A. Y. Takeuchi, I. L. Castro, and J. R. Proveti, Magnetic properties of NiMn-based Heusler alloys influenced by Fe atoms replacing Mn, J. Appl. Phys. **105**, 033919 (2009).

[64] X. Wang, M. M. Li, J. Li, J. J. Deng, Y. Wang, L. Ma, D. W. Zhao, C. M. Zhen, D. L. Hou, E. K. Liu, W. H. Wang, and G. H. Wu, Design of Mn-Mn distance for tunable spontaneous exchange bias in Heusler alloys, Intermetallics **132**, 107170 (2021).